Available online at www.sciencedirect.com
SCIENCE DIRECT®
ELSEVIER
Nuclear Instruments and Methods in Physics Research A 554 (2005) 1–12
NUCLEAR INSTRUMENTS & METHODS IN PHYSICS RESEARCH Section A
www.elsevier.com/locate/nima

Design and RF measurements of an X-band accelerating structure for linearizing the longitudinal emittance at SPARC

D. Alesini[a], A. Falone[b], M. Migliorati[a,b], A. Mostacci[a,b], F. Palpini[b], L. Palumbo[a,b,*], B. Spataro[a]

[a]*INFN-LNF Via E. Fermi 40, I-00044 Frascati, Italy*
[b]*Università degli Studi di Roma "La Sapienza", Dip. Energetica, Via A. Scarpa 14, 00161, Roma, Italy*

Received 10 June 2005; received in revised form 22 July 2005; accepted 24 July 2005
Available online 22 September 2005

Abstract

The paper presents the design of an X-band accelerating section for linearizing the longitudinal phase space in the Frascati Linac Coherent Light Source (SPARC). The nine cells structure, operating on the π standing wave mode, is fed by a central coupler and has been designed to obtain a 42 MV/m accelerating gradient. The two-dimensional (2D) profile has been obtained using the electromagnetic codes Superfish and Oscar-2D while the coupler has been designed using HFSS. Bead-pull measurements made on a copper prototype have been performed and the results are illustrated and compared with the numerical predictions. Mechanical details of the realized prototype and RF properties of the structure as a function of the assembly characteristics are also discussed.

PACS: 41.75.−i; 41.60.Cr

Keywords: High-brightness beams; Soft X-ray FEL

1. Introduction

The SPARC [1] injector aims to produce a high brightness electron beam able to drive a self-amplified spontaneous free-electron laser (SASE-FEL) experiment in the green visible light and to develop an ultra-brilliant beam photo-injector needed for the future SASE-FEL based X-ray sources. The SPARC photo-injector (Fig. 1) consists of 1.6 cell radio frequency (RF) gun of the BNL/UCLA/SLAC type [2] operating at S-band with incorporated metallic photo-cathode (Cu or Mg). The gun generates a 6 MeV electron beam to be then accelerated in two S-band, travelling wave sections (SLAC type). The beam

*Corresponding author. Dipartimento di Energetica, Università degli Studi di Roma "La Sapienza", Via A. Scarpa 14, 00161 - Roma, Italy. Tel.: +39 06 49766343; fax: +39 06 44240183.
E-mail address: luigi.palumbo@uniroma1.it (L. Palumbo).

0168-9002/$ - see front matter © 2005 Published by Elsevier B.V.
doi:10.1016/j.nima.2005.07.072

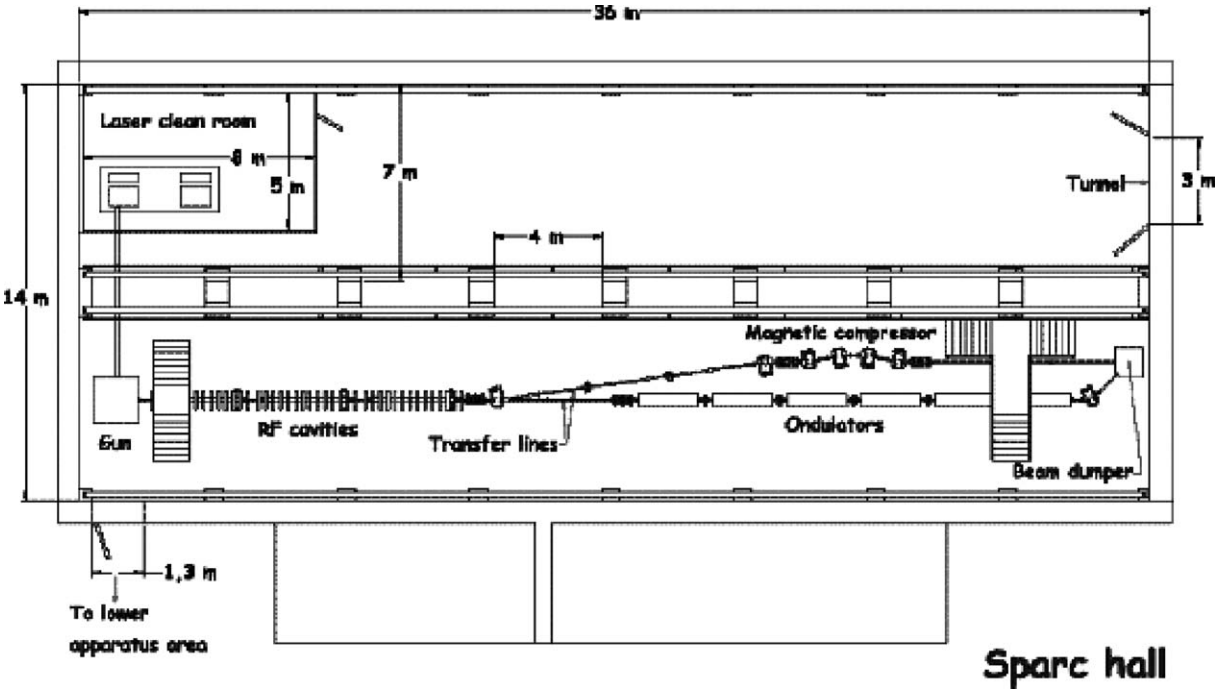

Fig. 1. SPARC photo-injector layout.

parameter list at the end of the injector is reported in Table 1.

In the SPARC phase II the first LINAC section, downstream the RF gun, will be used to study RF compression [3]. These tests of RF compression assume great relevance in the SPARC R&D program [4] since the general layout for SPARX [5] foresees the use of a mixed compression scheme: RF compression in the photo-injector up to 500 A and one single stage of magnetic compression at 1 GeV up to the final peak current of 1 kA. In this case the use of the X-Band structure operating at 11.424 GHz is required to compensate the non-linearity distortions due to the RF curvature during acceleration and compression [6]. The schematic layout is reported in Fig. 2. The X-Band structure, designed [7] to obtain 42 MV/m accelerating gradient, is a nine cells π-mode structure fed by a central coupler. The fourth harmonic of 2.856 GHz (instead of the third harmonic) has been chosen for space availability reasons and also because the technologies in the X-Band power sources and modulators have been already developed at KEK, SLAC and Varian [8–14] for future linear collider projects. The design of the accelerating section is described in Section 2. In the third paragraph of this paper

Table 1
Beam parameter list at the end of the SPARC injector

Electron beam energy (MeV)	155
Bunch charge (nC)	1.1
Repetition rate (Hz)	10
Cathode peak field (MV/m)	120
Peak solenoid field (T)	0.273
Photocathode spot size (mm)	1.13
Laser pulse duration (ps)	10
Bunch energy at gun exit (MeV)	5.6
Bunch peak current at linac exit (A)	100
RMS normalized transverse emittance at linac exit (mm mrad)	<2
RMS slice normalized transverse emittance at linac exit (300 μm) (mm mrad)	<1
RMS longitudinal emittance at linac exit (deg keV)	1000
RMS energy spread (%)	0.2
RMS bunch length at LINAC exit (mm)	1

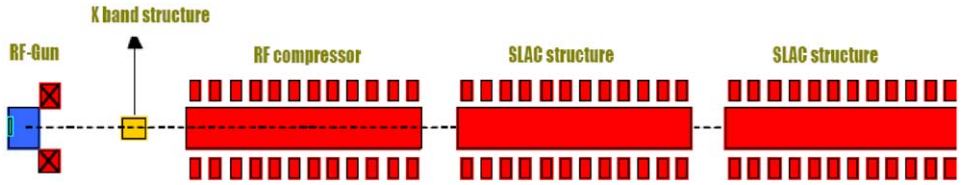

Fig. 2. Schematic layout of the photo-injector of SPARC phase II.

we describe the copper prototype and the measurement setup while the last section is devoted to the discussion of the RF measurement results.

2. The X band structure design

2.1. 2D profile

The detailed analysis of the structure design without coupler is reported elsewhere [7]. The single cell dimensions are reported in Fig. 3 and have been determined with the two-dimensional (2D) electromagnetic (e.m.) codes SUPERFISH [15] and Oscar-2D [16]. In particular the beam aperture diameter (r_2) has been fixed by beam dynamics requirements and the outer diameter (r) has been chosen to tune the resonance of the π-mode at 11.424 GHz.

The complete structure (without coupler) is reported in Fig. 4. The choice of 9 cells has been done to achieve a total accelerating voltage $V = 5$ MV with 3 MW of peak input power. The two cells connected to the beam pipe tube have different outer dimensions in order to compensate the detuning of the resonant frequency due to the presence of the beam pipe itself. No dedicated dampers of the parasitic higher order modes have been adopted since the X-Band structure operates on single bunch. The longitudinal electric filed on axis is reported in Fig. 5 while the cavity parameters are reported in Table 2.

2.2. Coupler design

Concerning the coupler design, it has been decided to feed the cavity in the central cell in order to not excite the mode $\frac{8}{9}\pi$ that has the frequency nearest to the π mode and no field in the central cell. Therefore with a central coupler we have a much greater separation of the modes and, therefore, the working mode is less perturbed by the closest one. To reduce the coupler window dimensions we have decided to taper the smaller dimension (10.16 mm) of the standard X-band waveguide (10.16 mm × 22.86 mm) to the dimension of 4 mm (Fig. 6). The coupling cell is sketched in Fig. 7.

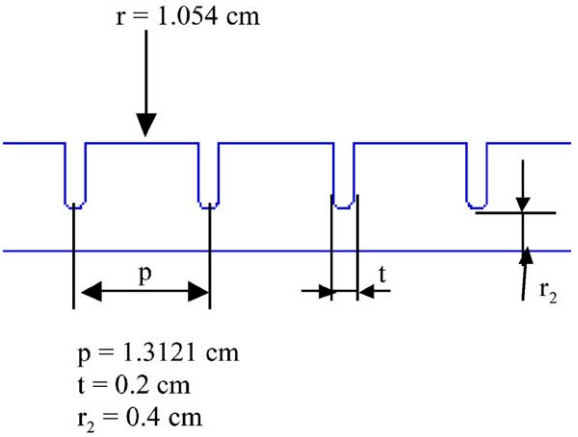

Fig. 3. Single cell dimensions of the π-mode X-band structure.

The dimension of the coupler window (w) and of the central cell radius (R_c) have been tuned in order to obtain simultaneously a coupling coefficient $\beta = 1$, a resonant frequency of the whole system (cells + coupler) equal to 11.424 GHz and to preserve a good field flatness. This has been done using the electromagnetic simulation code HFSS [17] by following two steps:

(1) We have simulated a single cell with coupler as shown in Fig. 8. To get a better accuracy results we have simulated only one quarter of the structure with the proper boundary

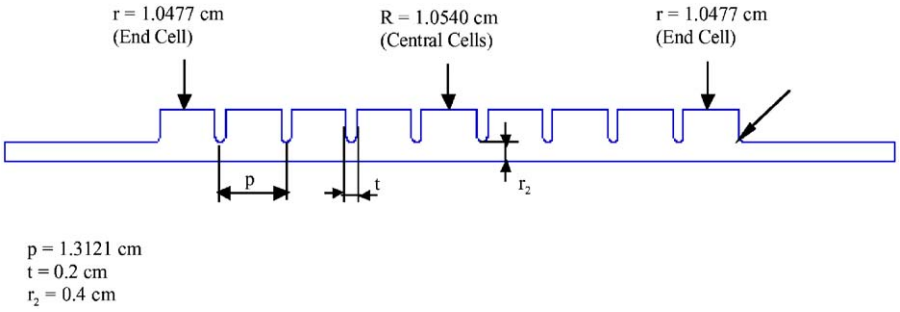

Fig. 4. Complete π-mode X-band structure without coupler.

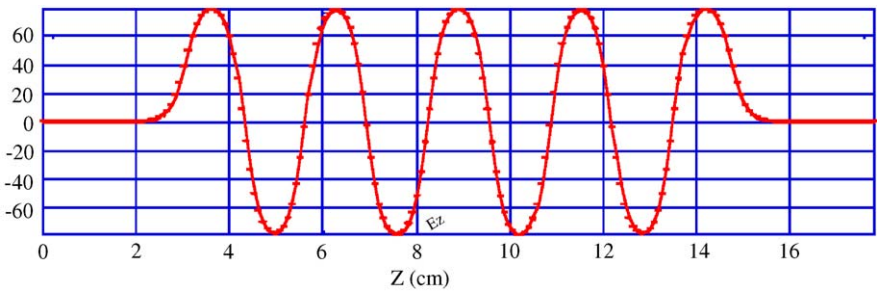

Fig. 5. Longitudinal electric field on axis (Superfish and Oscar 2D calculations).

Table 2
X-band cavity parameters (Superfish and Oscar 2D calculations)

Frequency (GHz)	11.424
Cells length (mm)	13.12
Number of cells	9
Beam holes radius r (mm)	4
Iris thickness t (mm)	2
Transit time factor T	0.731
Quality factor Q	8400
R/Q (Ω/m)	9165
Coupling coefficient K (%)	2.42
Peak input power P (MW)	2.7
Duty cycle	10^{-4}
Repetition frequency (Hz)	50
Average power dissipation P_d (W)	270
Peak axial electric field (MV/m)	57.5
Kilpatrick factor	1.197
Peak surface electric field (MV/m)	105

conditions. The dimensions of the coupler window and cell radius have been tuned in order to obtain a coupling coefficient $\beta = 9$ (exactly 9 times the coupling coefficient that we would reach with the complete structure) and a cell resonant frequency equal to 11.424 GHz.

(2) We have simulated the complete structure (one quarter of the structure as shown in Fig. 9) with the dimensions found in the previous case and we have slightly adjusted the dimensions of the coupler cell and window to obtain a good field flatness at the resonant frequency of 11.424 with $\beta = 1$.

The final cell coupler dimensions are reported in Fig. 7 and the obtained reflection coefficient at the coupler port and the electric field on axis are reported in Fig. 10. By fitting the reflection coefficient at the input coupler port with the formula:

$$|S_{11}| = \sqrt{\frac{\left(\frac{1-\beta}{1+\beta}\right)^2 + (Q_L\delta)^2}{1+(Q_L\delta)^2}}$$

$$\text{with } \delta = \frac{\omega}{\omega_{res}} - \frac{\omega_{res}}{\omega}, \quad Q_L = Q_{EXT}\frac{\beta}{1+\beta}$$

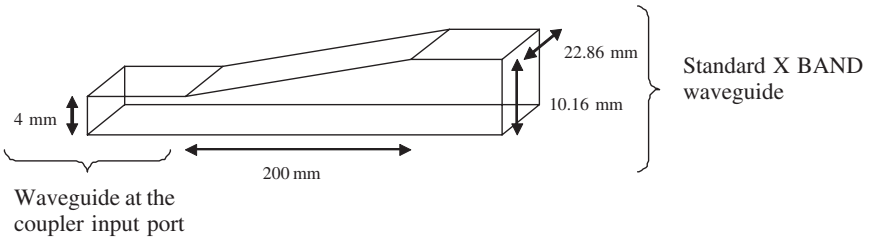

Fig. 6. Tapering between the standard X-Band waveguide and the coupler input port.

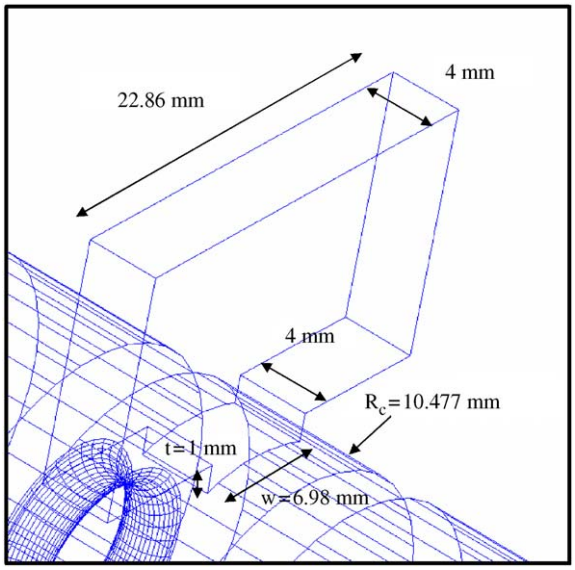

Fig. 7. Sketch of the coupling cell.

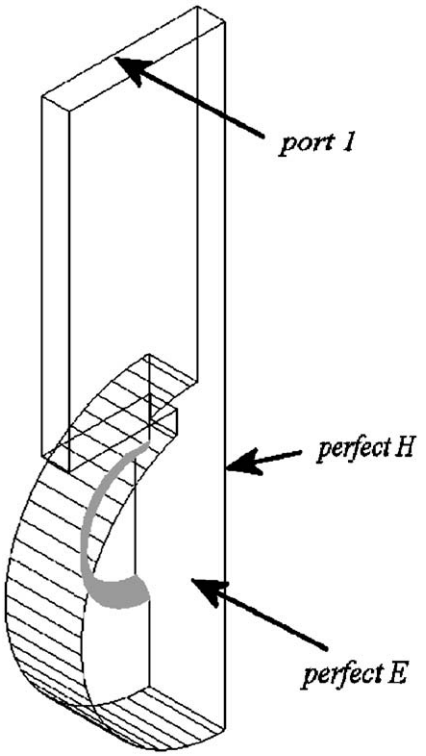

Fig. 8. Single cell with coupler simulated by HFSS.

we have obtained the external quality factor $Q_{EXT} = 7900$ and the coupling coefficient $\beta = 1.09$. The values of the simulated Q_{EXT} and field flatness could be optimized after measurement results.

3. Copper prototype and measurement setup

A full scale copper prototype has been constructed and is shown in Fig. 11. The detail of the mechanical drawing is reported in Fig. 12. The nine cells structure has been designed for brazing, but the RF tests refer to a mechanically joined structure. The material used to build this prototype is oxygen free copper. The structure has been realized by mechanical machining with a numerically controlled lathe and the obtained precision is below ± 0.01 mm, while the surface roughness is not worst than $0.4\mu R_a$. The surface finishing was obtained directly by mechanical machining with custom cutting tools, avoiding any polishing technique and only silicon and sulphur free cutting fluid was used. The final machining was done at

constant temperature in order to guarantee as much as possible the uniformity of the mechanical dimension of the cells. After machining, a standard cleaning procedure was performed using an alkaline solution at 3% at 50 °C followed by a rinse in tap water and a final rinse in distilled water followed by a chemical cleaning with citric acid solution and a rinse in tap water and finally a rinse in distilled water. Then the pieces were dried in a dust free oven. Each cell dimension has been checked with a quality control test.

The assembling procedure foresees the joining of the nine cells using two stainless steel disks used to press the structure by means of three 8 mm diameter copper rods. A torque of 5 Nm, corresponding to a pressure of roughly 80 N/mm^2, was applied. To feed the structure two lateral small antennas are placed.

Two types of different measurements have been carried out: transmission (or reflection) scattering coefficient measurement (between the two antennas or between the antennas and the central coupler) and bead pull measurements.

With the first type of measurements we have found the resonant frequency, the β coefficient at the input ports and the unloaded or external quality factors of π (or other) mode(s). With the second type of measurements we have found the longitudinal electric field on axis and we have calculated the shunt impedance of the structure.

The complete measurement setup is shown in Fig. 13. The PC controls both the network analyzer Agilent N5230A (interfaced by a GPIB Ethernet device) and the control circuit of the steeping motor through LABVIEW [18]. The nylon wire is kept straight by a 75 g weight.

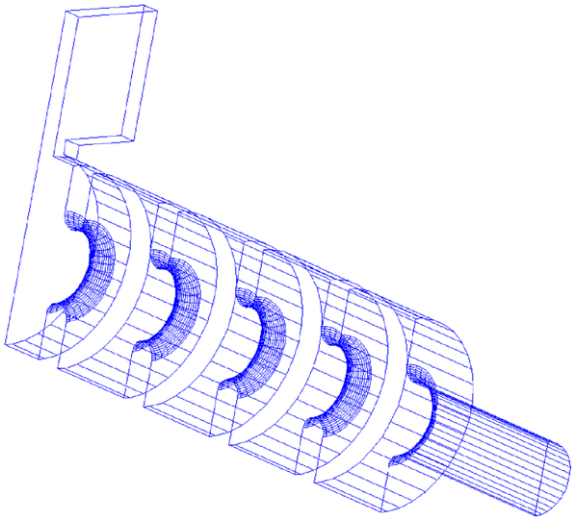

Fig. 9. Complete structure with coupler simulated by HFSS.

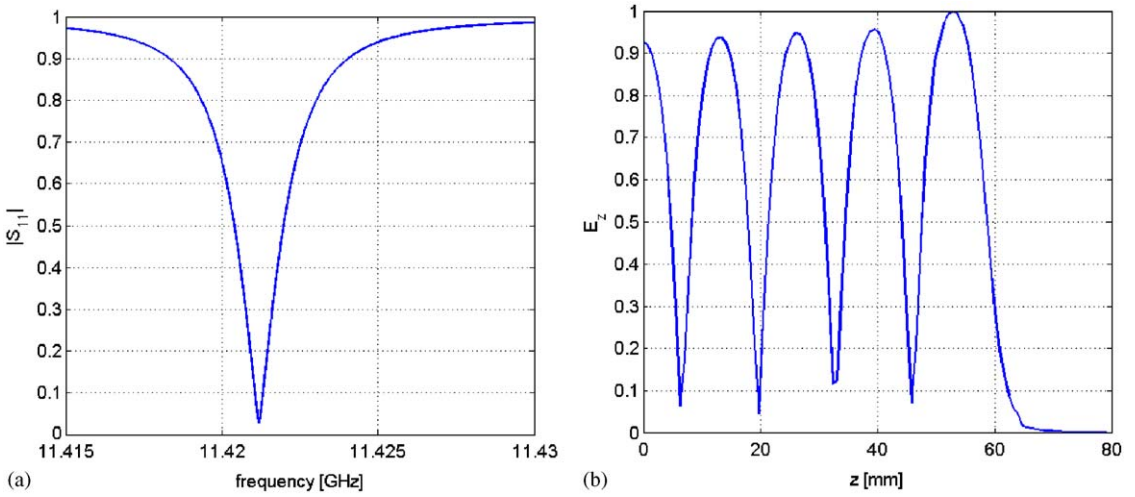

Fig. 10. Simulated reflection coefficient at the coupler port and normalized electric field on axis at the π-mode resonant frequency (HFSS simulations).

Fig. 11. Copper prototype of the X band structure.

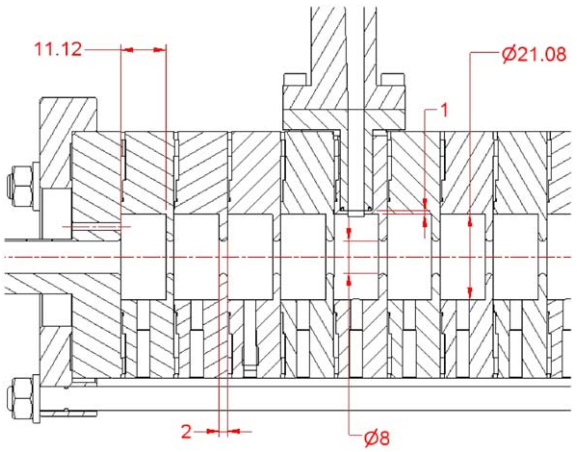

Fig. 12. Detail of the mechanical drawing.

4. Measurement results

4.1. Resonant frequency and quality factors measurements results

The transmission coefficient between the two small antennas and between the antenna and the central coupler are reported in Fig. 14a and b. As previously observed, we can excite only five over nine possible modes by the central coupler because we impose a non-zero field in the central cell. On the contrary with the two antennas we can excite all the possible modes. The measured dispersion curve, compared with the one obtained from HFSS and SUPERFISH, is reported in Fig. 15.

The quality factor of the resonance has been measured as a function of pressure realized by the rods. The results are reported in Fig. 16. As expected the Q factor increases with the increasing pressure and, with the maximum pressure, we have obtained the result reported in Table 3 and compared with the numerical one. These results prove that even if the structure is not brazed the electric contact is good enough to have a Q-factor of the resonance comparable with the numerical one. Concerning the external quality factor it has been found the value $Q_{EXT} = 8000$ in agreement with the simulation results.

4.2. Electric field measurement results

The bead-pull technique that we have used is based on the Slater theorem and is widely discussed elsewhere [19]. The small perturbing object inside the cavity induces a frequency shift that is related to the variation of the electric and magnetic energy stored in the cavity in the point where the object is located according to the

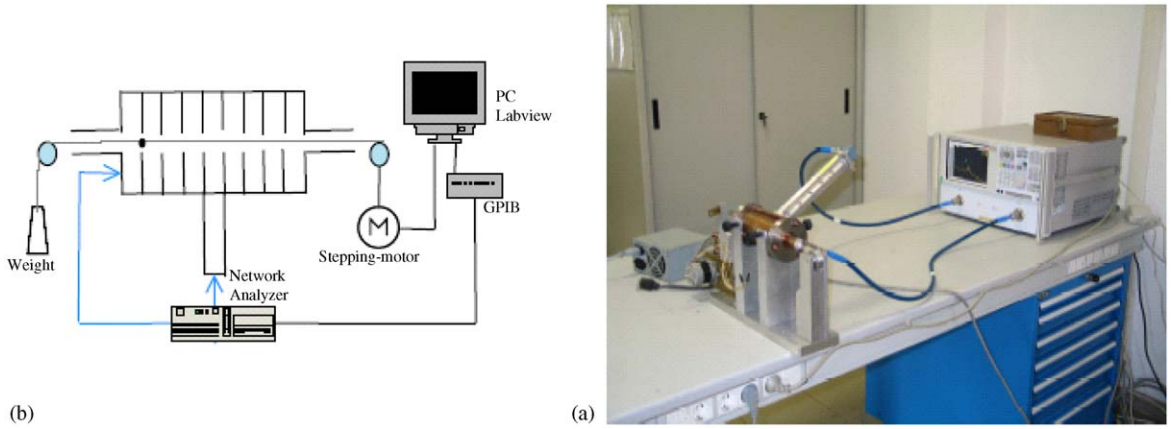

Fig. 13. Picture of the measurement setup (b) and conceptual scheme (a).

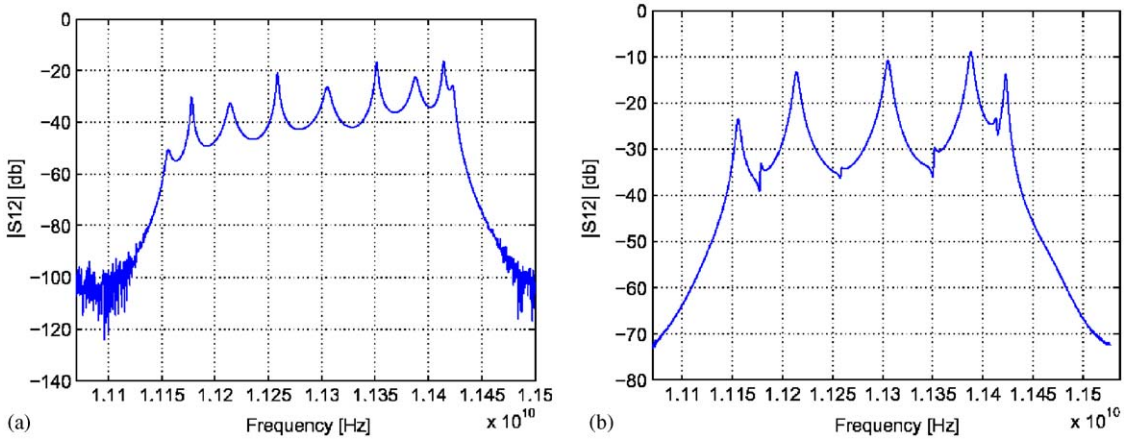

Fig. 14. Transmission coefficients between the two small antennas (a) and between the antenna and the central coupler (b).

formula:

$$\frac{\omega_p-\omega_0}{\omega_0}=\frac{1}{4U}\int_{\Delta V}(\mu_0|\vec{H}|^2-\varepsilon_0|\vec{E}|^2)\,\mathrm{d}V.$$

Considering the accelerating mode and the small transverse dimensions of the perturbing object (of the order of 0.1 mm) it is possible to find the longitudinal electric field on axis by the formula:

$$\frac{\omega_p-\omega_0}{\omega_0}=-\varepsilon_0 k_e\Delta V\frac{E_z^2}{4U}=\frac{1}{2Q_L}\tan(\phi(f_0))$$

where k_e is the form factor of the object, ΔV is the perturbing object volume, U the total energy stored in the cavity, Q_L is the loaded quality factor of the resonance and $\phi(f_0)$ is the phase of the transmission coefficient between two ports coupled with the field in the cavity. The latest expression have been written because it is more convenient to measure the phase shift of the resonant frequency instead of $\Delta\omega$ [20]. Moreover, for $\phi(f_0)$ reasonably small (e.g. smaller than 30°), $\tan(\phi)$ is approximately equal to ϕ and this has some practical advantages. The perturbing objects are cylinders made of copper

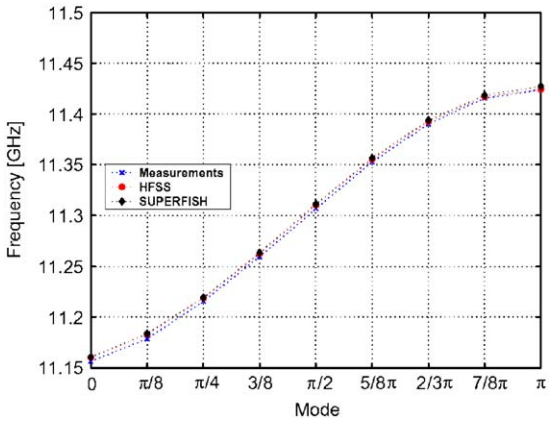

Fig. 15. Measured dispersion curve, compared to HFSS and SUPERFISH results.

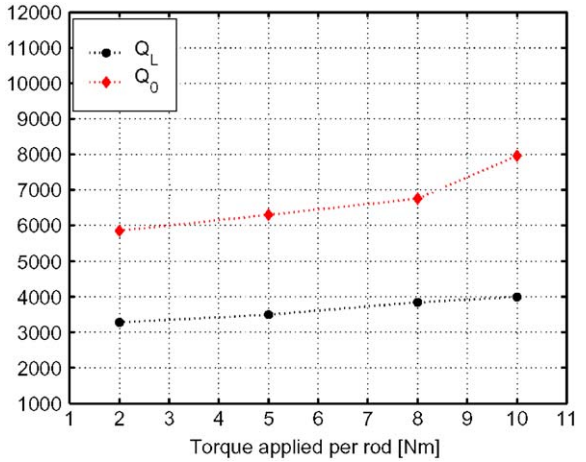

Fig. 16. Measured quality factor of the π mode resonance as a function of pressure realized by the rods.

Table 3
Unloaded quality factor measured with the maximum pressure and compared with the numerical results

	HFSS	SUPERFISH	OSCAR 2D	Measurements
Q_0	8500	8070	8413	7960

with a radius of 0.09 mm and length of 0.7 and 0.9 mm (measured with a digital callipers with an uncertainty of 10 μm).

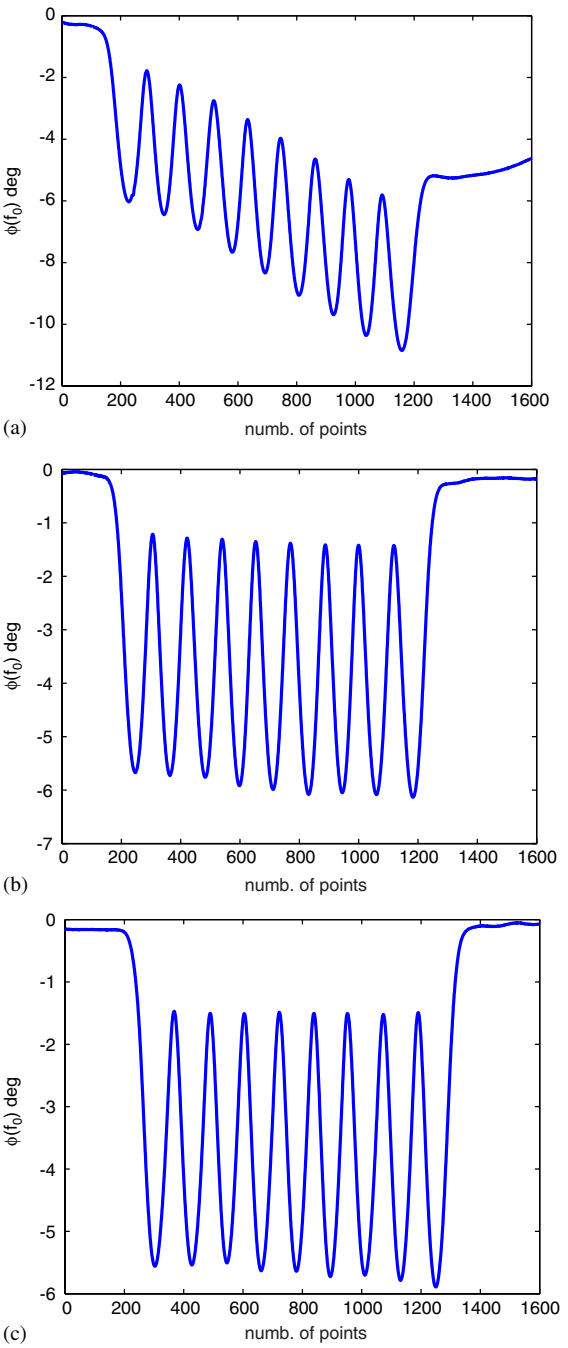

Fig. 17. Phase of resonance measurement with different wire diameters: (a) 0.18 mm; (b) 0.148 mm; (c) 0.083 mm.

A careful optimization of the measurement setup has been done in order to minimize the systematic errors and to better understand the

uncertainty of the measurements. The most important reasons of induced errors in the measurements were:

(1) The effect of wire nylon that induced an unwanted perturbation in the frequency measurement. To cancel this systematic error different measurements have been done with different nylon wire diameters. A typical phase resonance measurement with different wire diameters is reported in Fig. 17. The best results have been obtained with the smallest wire and the final small systematic error has been completely cancelled considering the frequency shift with and without the perturbing object. As example in Fig. 18 it is reported the results of phase shift considering different pieces of nylon wire with the smallest diameter of 0.083 mm without perturbing object.
(2) The effect of the drops of glue used to fix the perturbing object. It gave a perturbation in the frequency measurement of the order of 10% of the total frequency variation. In particular the frequency variation at the center of the irises did not go to zero. To take into account this effect different measurements have been done in order to subtract the systematic perturbation to the measure as shown in Fig. 19.
(3) The effect of jitter in the longitudinal coordinate between different measurements and within a single measure. This problem, given by the stepping motor, has been reduced using a weight smaller than 75 g, and correcting off-line the measurement results. As example in Fig. 20 it is reported the result of two different measurements.

To calculate the R/Q of the structure it has been necessary to determine the form-factor of the different perturbing objects. In literature there are many analytical formulas for the determination of the form-factor for ellipsoid geometries [21]. The used perturbed objects are far to be perfect ellipsoid and we have preferred to determine the form factor through experimental calibration [22]. Using Slater's theorem we can calibrate the form factor comparing the perturbation induced by the perturbing object in a cavity with known field. For this purpose, it has been used a pill-box cavity working at 1.91 GHz on the TM_{010} mode. Using different resonant mode of the pillbox cavity we have also checked that the form-factor does not depend on the frequency. The results of this calibration are reported in Table 4 where the obtained form factors of two objects with different length are reported [23].

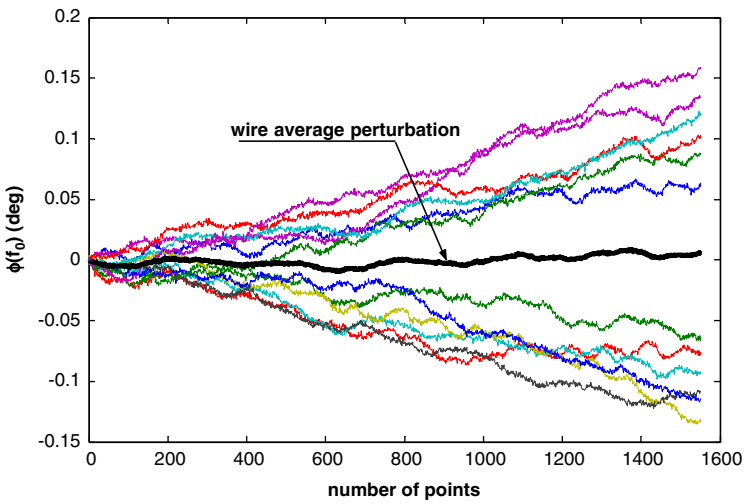

Fig. 18. Resonance phase shift considering different pieces of nylon wire with the smallest diameter of 0.083 mm.

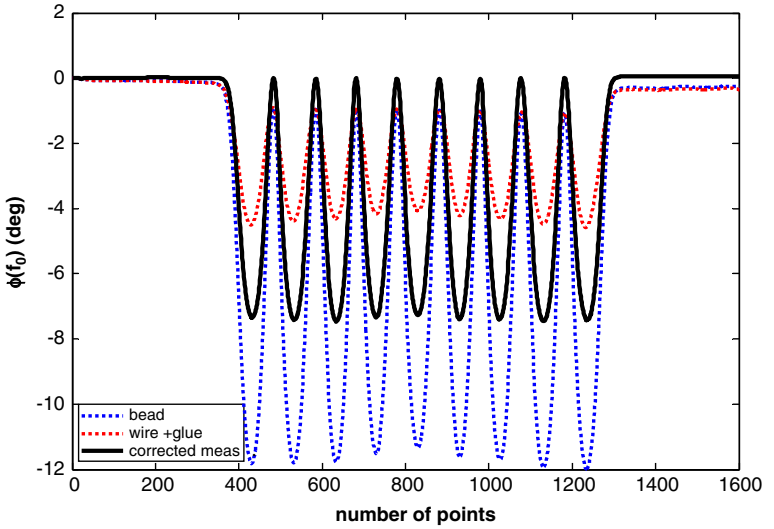

Fig. 19. Phase measurement taking into account the effect of the wire and of the glue.

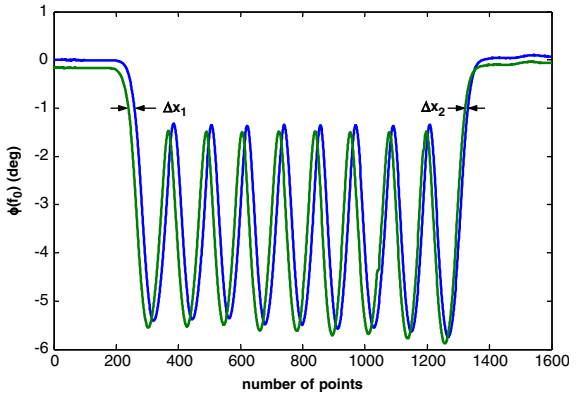

Fig. 20. Jitter between two different measurements.

Table 4
Form factors obtained by calibration of two objects with different length

Object length (mm)	Form factor k_e	R/Q (Ω/m)
0.7	25.860 ± 0.031	9480 ± 96
0.9	28.400 ± 0.027	9367 ± 211

The measured longitudinal electric field on axis, after the tuning procedure, is plotted in Fig. 21. The reached field-flatness is of the order of 1% at the nominal resonant frequency of 11.424 GHz. The calculated R_{sh}/Qs normalized to the cavity length are reported in Table 4 and they are in a very good agreement with the simulation results.

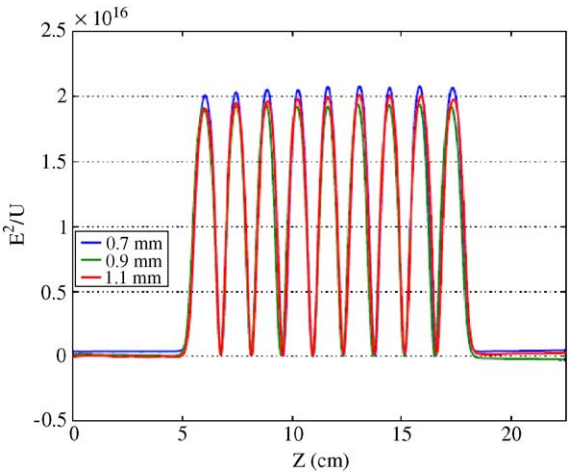

Fig. 21. Measured longitudinal electric field on axis.

5. Conclusions

In the paper we have presented the design of the X-band accelerating section for linearizing the longitudinal phase space in the Frascati Linac Coherent Light Source (SPARC). The structure,

operating on the π standing wave mode, is a 9 cells structure fed by a central coupler and has been designed to obtain a 5 MV accelerating voltage. Quality factors, resonant frequency and electric field measurements have been done on a copper prototype. Even if the prototype is not brazed the reached quality factors are very close to the theoretical ones. Concerning the electric field measurement with the bead pull technique we have discussed the most important reasons of induced errors and how to cancel these effects. In particular the effect of wire nylon, drops of glue used to fix the perturbing object and the effect of jitter in the longitudinal coordinate have been discussed. To calculate the R/Q factors the perturbing objects have been calibrated with a pill-box cavity and the final results are in very good agreement with the numerical ones.

Brazing tests are now in progress in the LNF for the construction of the final device.

Acknowledgements

The authors are grateful to P. Chimenti, V. Chimenti, A. Clozza and V. Lollo for their help in the mechanical design of the cavity prototype and to A. Bacci for the SUPERFISH simulations.

References

[1] Technical Design Report for the SPARC Advanced Photo-Injector, Technical Report, LNF-INFN, ROMA, 2003.
[2] D.T. Palmer, The next generation photoinjector, Ph.D.Thesis, Stanford University.
[3] M. Ferrario, et al., Homdyn Study for the LCLS RF Photoinjector, SLAC-PUB 8400.
[4] D. Alesini, et al., Conceptual design of a high-brightness linac for soft X-ray SASE-FEL source, these proceedings.
[5] D. Alesini, et al., The SPARX study group, Nucl. Instr. and Meth. A 507 (2003) 502.
[6] P. Emma, X-band RF harmonic compensation for the linear bunch compression in the LCLS, SLAC, LCLS-TN-01-1, 2001.
[7] A. Bacci, et al., An X-band structure for a longitudinal emittance correction at SPARC, SIS-Pubblicazioni, LNF-INFN, LNF 03/008(R), 2003.
[8] K. Takata, Proceedings of the First Workshop on Japan Linear Collider (JLC), KEK, October 24–25, 1989.
[9] J.W. Wang, G.A. Loew, Measurements of Ultimate Accelerating Gradients in the SLAC Disk-loaded Structure, 1985 PAC, Vancouver, BC, May 1985, SLAC-PUB-3597, March 1985.
[10] J.W. Wang, V. Nguyen-Tuong, G.A. Loew, RF breakdown studies in a SLAC diskloaded structure, Proceedings of the 1986 Linear Accelerator Conference, Stanford, CA, June 1986, SLAC-PUB-3940, April 1986.
[11] J.W. Wang, G.A. Loew, Progress report on new RF breakdown studies in an S-band structure at SLAC, Presented at the 1987 PAC, Washington, DC, March 1987, SLAC-PUB-4247, February 1987.
[12] E. Tanabe, J. W. Wang, G.A. Loew, Voltage breakdown at X-band and C-band frequencies, Proceedings of the 1986 Linear Accelerator Conference, Stanford, CA, June 1986.
[13] J.W. Wang, RF properties of periodic accelerating structures for linear colliders, SLAC Report-339, July 1989.
[14] J.R. Rees, A perturbation approach to calculating the behavior of multi-cell radiofrequency accelerating structures, PEP-255, Stanford Linear Accelerator Centre, 1976.
[15] J.H. Billen, L.M. Young, Part. Accel. 7 (4) (1976) 213.
[16] P. Fernandes, R. Parodi, LALAGE—A computer program to calculate the TM modes of cylindrically symmetrical multicell resonant structures, PAC 1982, vol. 12, pp. 131.
[17] http://www.ansoft.com.
[18] http://www.ni.com/labview/.
[19] J.C. Slater, L.C. Maier, J. Appl. Phys. 23 (1) (1952) 68.
[20] P.J. Petersana, S.M. Anlage, J. Appl. Phys. 84 (6) (1998) 3392.
[21] G. Dome, F. Caspers, Precise perturbation measurement of resonant cavities and higher mode identification, Cern SPS/85-46, 1984.
[22] J.C. Slater, Microwave Electronics, Dover Publication, New York, 1969.
[23] International Organization for Standardization et al., Guide to the expression of uncertainty in measurement, ISO, Geneva, 1995.